Supporting Information

Bioderived Silicon Nano-quills: Synthesis, Structure and Performance in Lithium-ion Battery Anodes

Nancy Chen [a, 1], Morteza Sabet [a, b, 1 *], Nawraj Sapkota [b, c], Mihir Parekh [b, c], Shailendra Chiluwal [b, c], Kelliann Koehler [d], Craig M. Clemons [a, e], Yi Ding [f], Apparao M. Rao [b, c *], Srikanth Pilla [a, g, h, i, j *]

[a] Department of Automotive Engineering, Clemson University, Greenville, SC, USA

[b] Clemson Nanomaterials Institute, Clemson University, Anderson, SC, USA

[c] Department of Physics and Astronomy, Clemson University, Clemson, SC, USA

[d] Electron Microscopy Laboratory, Clemson University, Anderson, SC, USA

[e] USDA Forest Service, Forest Products Laboratory, Madison, WI, USA

[f] U. S. Army DEVCOM GVSC, Warren, MI, USA

[g] Center for Composite Materials, University of Delaware, Newark, DE, USA

[h] Department of Mechanical Engineering, University of Delaware, Newark, DE, USA

[i] Department of Materials Science and Engineering, University of Delaware, Newark, DE, USA

[j] Department of Chemical and Biomolecular Engineering, University of Delaware, Newark, DE, USA

[1] Author contributed equally to this work.

* Corresponding authors: spilla@udel.edu, ssabet@clemson.edu, arao@clemson.edu

Supporting information contains the following details:

Number of pages: 20

Number of tables: 1

Number of figures: 13

DISTRIBUTION STATEMENT A. Approved for public release: distribution is unlimited.
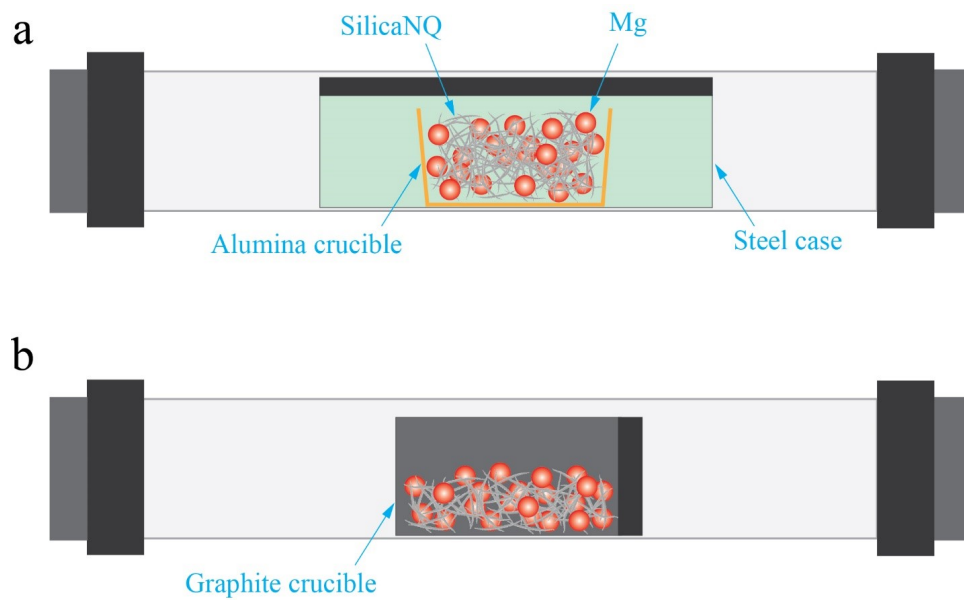*OPSEC #8228*

Figure S1: Schematic setup for magnesiothermic reduction of SilicaNQ using (a) an alumina boat and (b) a cylindrical graphite crucible.
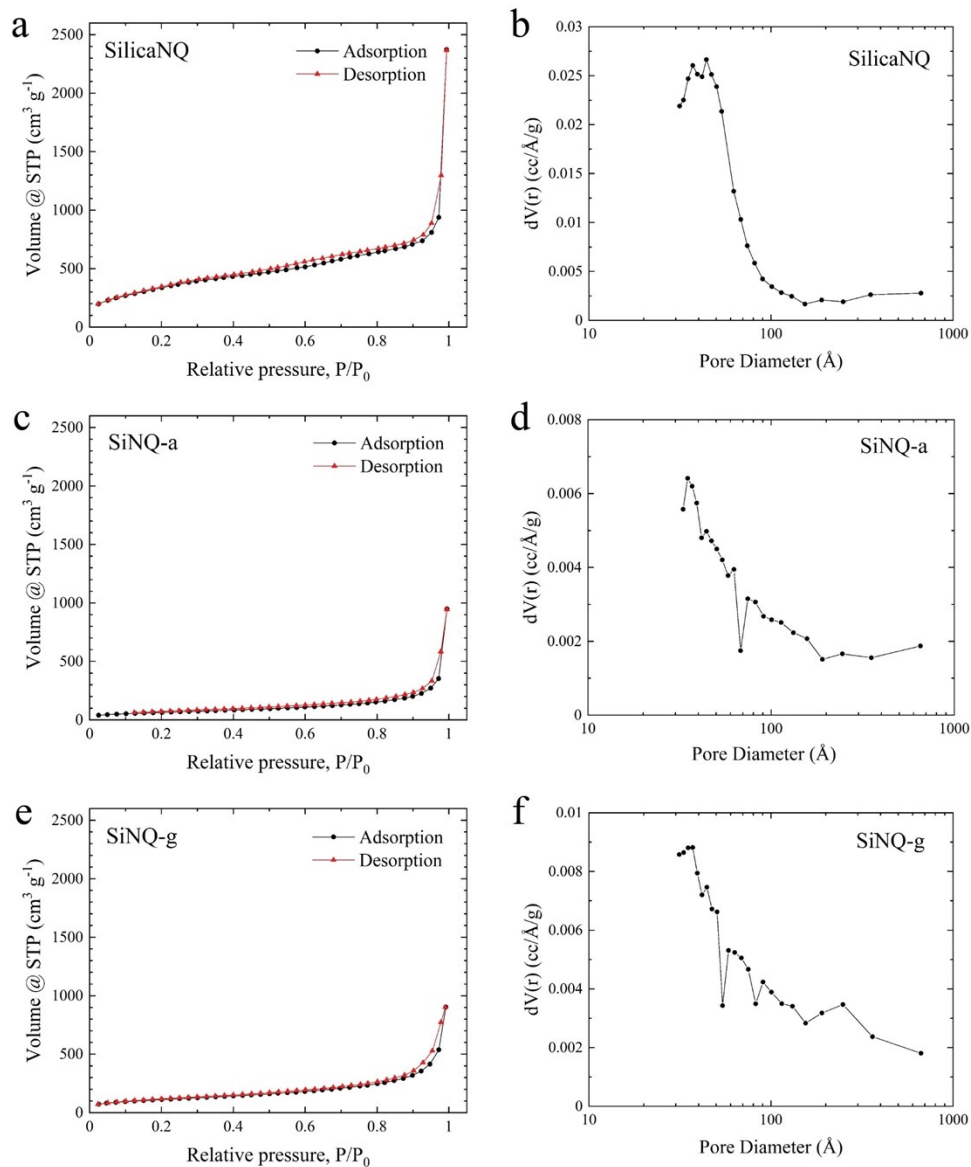
Figure S2: Gas physisorption measurements of nano-quill materials in this study; (a), (c), and (e) show adsorption-desorption isotherms, and (b), (d), and (f) illustrate pore size distributions. The BET method was used to estimate the specific surface area of materials. The total pore volume and pore size distribution of materials were evaluated by the BJH method.
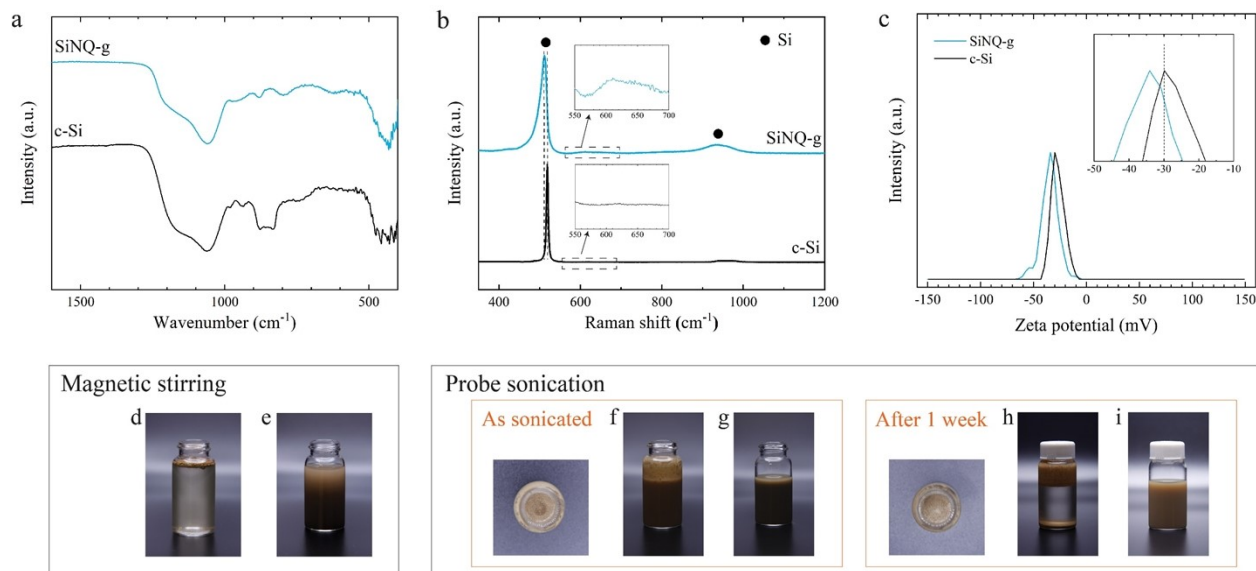
Figure S3: (a) FTIR and (b) Raman spectra of SiNQ-g and c-Si materials. Characteristic peaks show the presence of surface functional groups for SiNQ-g, which are absent for c-Si. (c) Zeta potential results of as-sonicated SiNQ-g and c-Si powders in DI water. Dispersion of SiNQ-g and c-Si in DI water using magnetic stirring and probe ultrasonication methods shows that (d) c-Si cannot be dispersed by stirring, while (e) SiNQ-g is easily dispersed after stirring for a short period. Probe sonication of (f) c-Si results in a partial dispersion (remaining c-Si float on top of the water), but (g) SiNQ-g is uniformly dispersed in water after a few seconds of probe sonication. After one week, (h) as-sonicated c-Si gets separated entirely, and (i) SiNQ-g suspension remains stable.
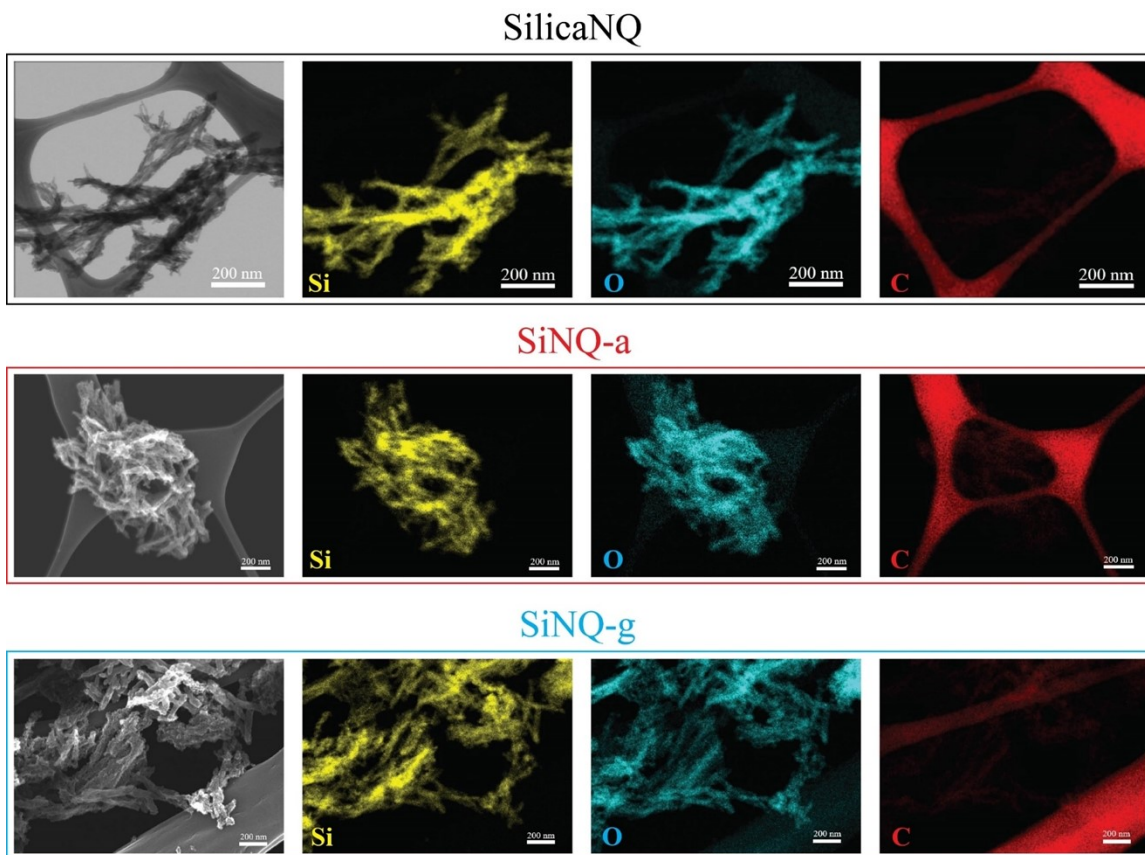
SilicaNQ

SiNQ-a

SiNQ-g

Figure S4: S-TEM elemental mapping of nano-quill materials in this study. The elemental maps related to Si, O, and C are illustrated here. The carbon maps are from the lacey carbon structure from the TEM grid.
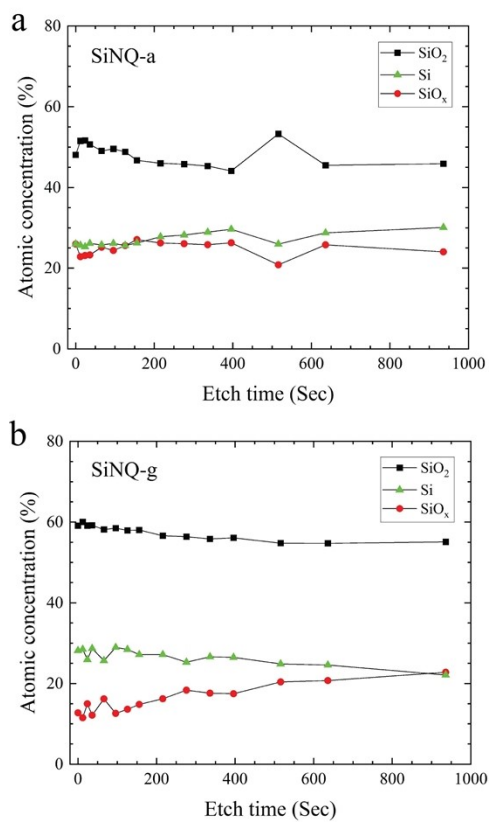
Figure S5: Atomic concentration of different Si-containing species in SiNQ-a and SiNQ-g materials as a function of XPS etch time.
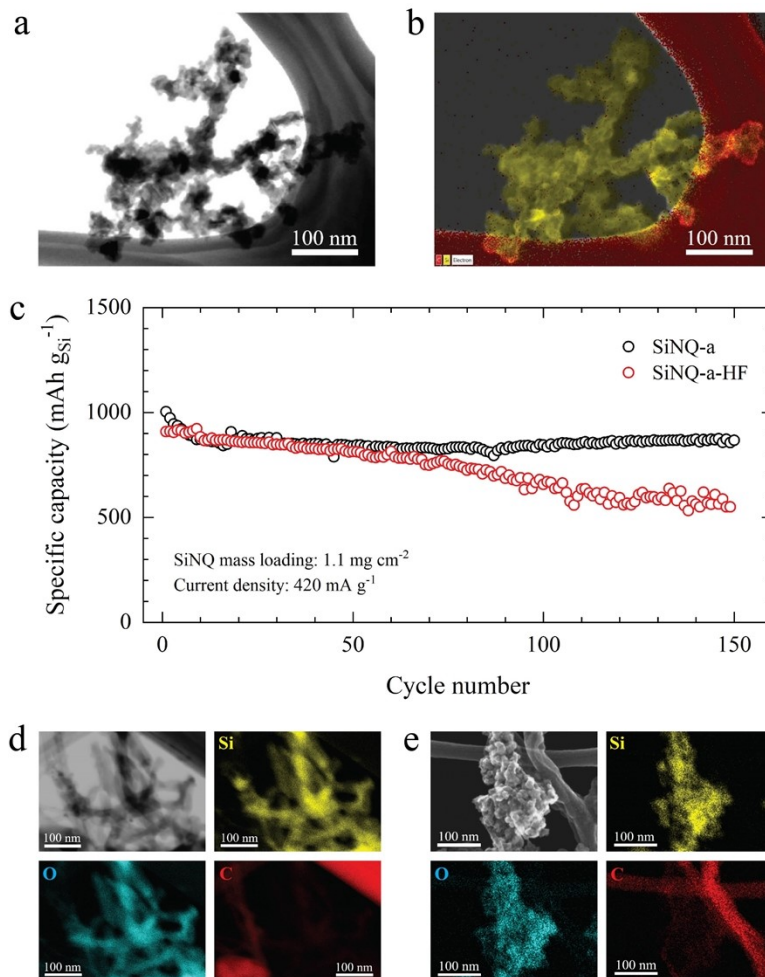
Figure S6: (a) S-TEM micrograph of HF-etched SiNQ-a, and (b) corresponding elemental maps for Si (yellow) and C (red). The O-containing species are removed from the structure by acid treatment of the as-reduced product using HF. (c) Electrochemical cycling results of anodes prepared using SiNQ-a (HCl etched) vs. SiNQ-a-HF (HCl and HF etched) active material. The electrodes were prepared by casting a slurry of each active material onto a conductive Bucky Paper current collector. Half cells were assembled and cycled between 1.0 V and 0.01 V at 0.1C (1C = 4200 mA g^{-1}). The delivered capacity was normalized by the mass of active material. (d) S-TEM micrograph and corresponding elemental maps of SiNQ-a anode after 150 cycles, and (e) S-TEM micrograph and corresponding elemental maps of SiNQ-a-HF anode after 150 cycles. It is evident that HCl-treated SiNQ maintained its 1D morphology after cycling.
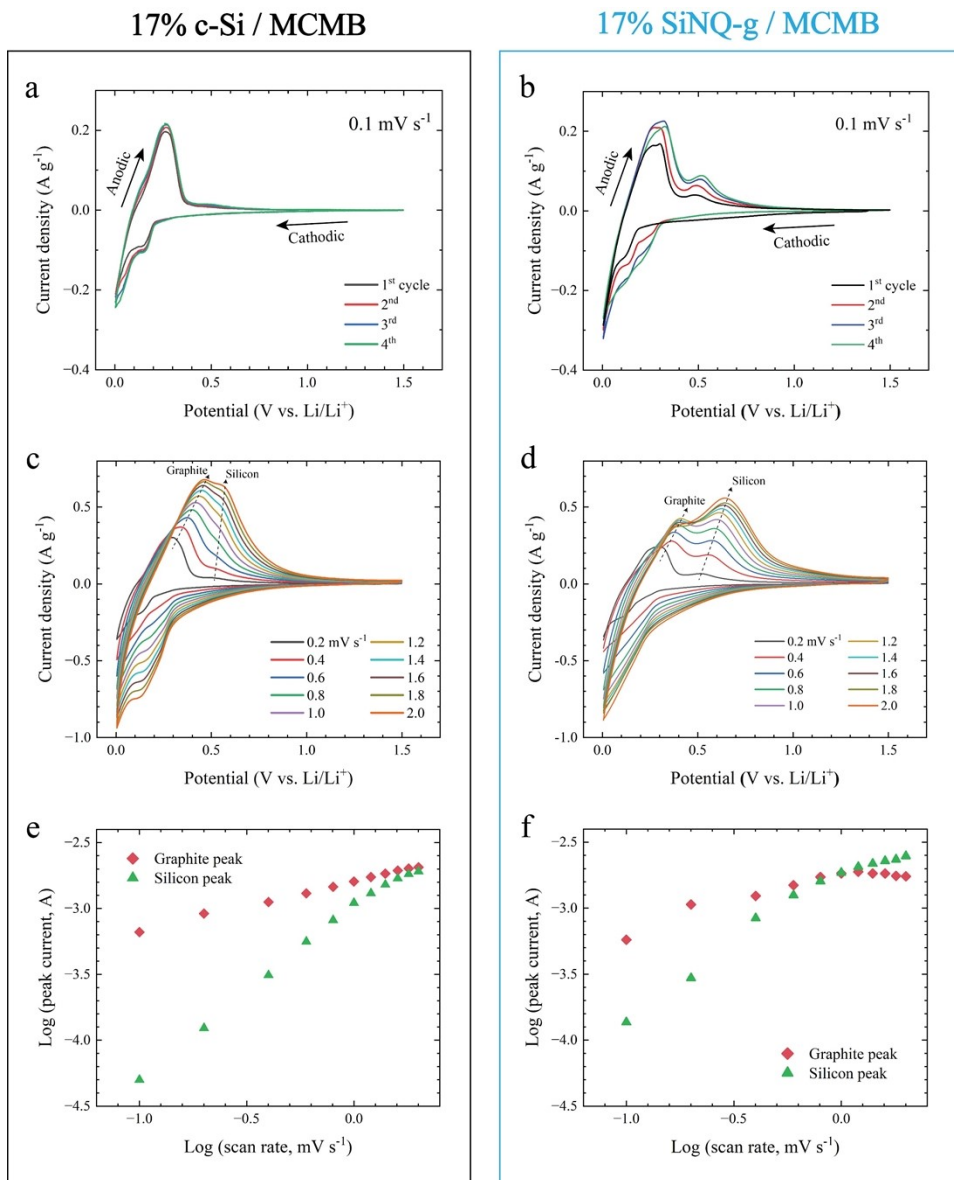
17% c-Si / MCMB   17% SiNQ-g / MCMB

Figure S7: Cyclic voltammetry of 17% c-Si/MCMB and 17% SiNQ-g/MCMB anodes. The anodic scan at 0.1 mV s⁻¹ is characterized by graphite delithiation peak at around 2.5-3.0 V and silicon delithiation peak at around 0.5 V. These two peaks are evolving at higher scan rates, with different behaviors for c-Si and SiNQ-g.

Cyclic voltammetry: A model to explain the dominant peak shift in Si-graphite electrodes

Within the electrode's active particle (Figure S8),

$$\frac{\partial C}{\partial t} = D \frac{1}{r^p \partial r} \frac{\partial}{\partial r}\left(r^p \frac{\partial C}{\partial r}\right),$$

(S1)

where $p = 1$ and 2 for cylindrical and spherical coordinates, respectively. The initial concentration before the start of cyclic voltammetry is given by,

$$C(r, t = 0) = C_0.$$

(S2)

Assuming the voltage scan rate as v and the initial voltage just before the start of CV as E_i gives,
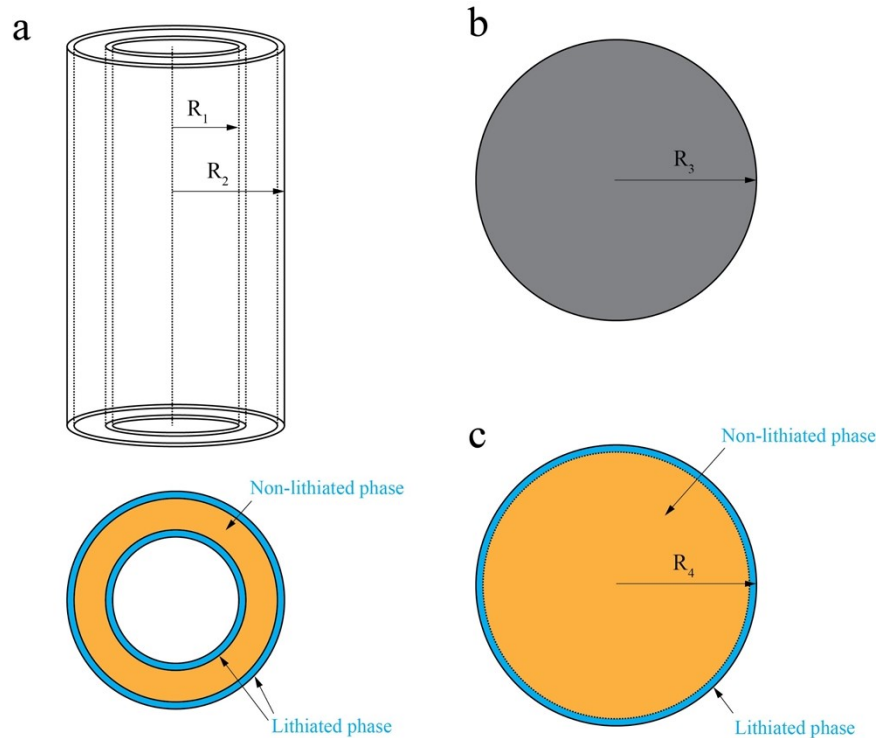
$$E = E_i + vt.$$

(S3)

Figure S8: Schematic representation of (a) SiNQ-g, (b) MCMB, and (c) c-Si particles. Particle sizes are not to scale.

For SiNQ-g particles (Figure S8a):

At the particle-electrolyte interface,

$$- AD\frac{\partial C}{\partial r}\Big|_{r = R_a} = \frac{i}{F},$$

(S4)

where i is the areal current density given by

$$i = \frac{i_1 \rho (R_2^2 - R_1^2)}{2 F R_a},$$

(S5)

where $a \in \{1,2\}$, $A = -1^a$, i_1 is the specific current density and ρ is the density. The electrochemical reaction kinetics is governed by the Butler-Volmer equation as

$$i_1 = i_0 \frac{2 F R_a}{\rho (R_2^2 - R_1^2)} \left(\frac{C(r = R_a)}{C_0} \exp\left(\frac{(1-\alpha)F\eta}{RT}\right) - \exp\left(-\frac{\alpha F\eta}{RT}\right) \right),$$

(S6)

where i_0 is the exchange current density, R is the universal gas constant, T is the temperature, α is the transfer coefficient, and η is the overpotential. We assume that the diffusion within the solid electrode particle is the rate-limiting step that governs the rate of delithiation, and that the diffusion within the electrolyte is much faster than that within the electrode.

For MCMB and c-Si spherical particles (Figures S8b, c):

At the particle-electrolyte interface,

$$- D\frac{\partial C}{\partial r}\Big|_{r = R_a} = \frac{i}{F},$$

(S7)

where i is the areal current density given by

$$i = \frac{i_1 \rho R_a}{3F},$$

(S8)

where $a \in \{3,4\}$, i_1 is the specific current density and ρ is the density. The electrochemical reaction kinetics is governed by the Butler-Volmer equation (diffusion within the solid electrode is assumed to be the rate limiting step) as

$$i_1 = i_0 \frac{3F}{R_a} \left(\frac{C(r = R_a)}{C_0} \exp \left(\frac{(1-\alpha)F\eta}{RT} \right) - \exp \left(-\frac{\alpha F\eta}{RT} \right) \right).$$

(S9)

For SiNQ-g, c-Si, and MCMB, the overpotential η is given by,

$$\eta = E - E_{eq}$$

(S10)

where $E_{eq} = E^0 - \frac{RT}{F} \ln(a_l(r = R_a))$ (the Nernst relation for equilibrium potential), with a_l being the activity of lithium ions within the electrolyte.

Why does the dominant peak shift?
For peak currents,

$$\frac{\partial i}{\partial t} = 0 = \frac{\partial (D \frac{\partial C}{\partial r}|_{r = R_a})}{\partial t}.$$

(S11)

For SiNQ-g, we assume that the peak current is reached simultaneously at both the inner and outer surfaces (R_1 and R_2). Since the peak shift happens at higher scan rates, where the overpotential is expected to be high, the electrochemical reaction almost becomes irreversible from quasi-reversible. Hence, we assume that the second term within parenthesis in Equations S6 and S9 is negligible compared to the first term. Using Equations S6, S9 – S11, and the Nernst relation for equilibrium potential, we get

$$\left|\frac{i_{peak}}{F}\right| = \left(\frac{(1-\alpha)Fv C}{RT}\Big|_{r=R_a} + D\frac{\partial^2 C}{\partial R^2}\Big|_{r=R_a}\right)\frac{R_a}{p},$$

(S12)

where $a \in \{1, 2, 3, 4\}$ and $p = 1$ for cylindrical coordinates (SiNQ-g) and 2 for spherical coordinates (MCMB and c-Si). A close look at Equation S12 suggests that the peak current has two components, namely, the pseudocapacitive component (i.e., the first term on the right side of Equation S12) and the diffusive component (i.e., the second term on the right side of Equation S12). The pseudocapacitive component is directly proportional to the voltage scan rate, and the relative contribution of the pseudocapacitive component is expected to increase with the scan rate. An order of magnitude analysis, shown below, of the two components suggests that the contribution of the pseudocapacitive component might exceed that of the diffusive component at scan rates greater than ~12.92 mV s^{-1}. The higher the contribution of the pseudocapacitive component, the larger the likelihood of the current peak shifting to a component with a larger *specific surface area*.

Order of magnitude analysis:
$$\frac{(1-\alpha)Fv C}{RT} \sim D\frac{C}{R_a^2}$$

(S13)

So, the pseudocapacitive term will become larger than the diffusive term approximately at a scan rate v given by

$$v \sim \frac{DRT}{FR_a^2(1-\alpha)}.$$

(S14)

Substituting the typical values of $D \sim$1E-16 m^2 s^{-1},[1] $R = 8.314$, $T = 300$ K, $F = 96500$ C mol^{-1}, α =0.5, and $R_a = 20$ nm gives $v \sim$12.92 mV s^{-1}. Experimental results in Figures S7c, d indicate that the peak shift takes place at ~0.8 mV s^{-1} for 17% SiNQ-g/MCMB anode and at >2.0 mV s^{-1} for 17% c-Si/MCMB anode. So, the theoretically predicted and experimentally observed scan rates for the peak shift are within the ballpark.

Given the fact that the specific surface area of SiNQ-g (~400 $m^2 g^{-1}$) and that of c-Si (~80 $m^2 g^{-1}$) are larger than MCMB's specific surface area (~2 $m^2 g^{-1}$), the shifting of the dominant peak from MCMB at lower scan rates to SiNQ-g and c-Si at higher scan rates is inevitable. Since the specific surface area of SiNQ-g is much larger than that of c-Si (around 5 times), the peak shift is observed earlier in 17% SiNQ-g/MCMB composite electrodes (~0.8 mV s^{-1}) compared to 17% c-Si/MCMB electrodes (>2 mV s^{-1}). The shifting of the dominant peak to SiNQ-g at higher scan rates indicates that SiNQ-based electrodes might be viable for fast-charging batteries because (a) silicon's theoretical capacity is higher than that of graphite, so it is advantageous to have SiNQ-g contribute more to the total current at higher scan rates as increased contribution of SiNQ-g indicates potential for higher capacities even during fast charging-discharging, and (b) SiNQ-g has demonstrated remarkable capacity retention. This has further been demonstrated in fast charging-discharging tests, the results of which have been depicted in Figures 4d and S12. While it seems that the pseudocapacitive component scales linearly with the scan rate, this apparent linear relation would be valid only if the concentration at the electrode-electrolyte interface is independent of the scan rate. Additionally, the diffusive term does not seem to be explicitly related to voltage scan rate. Thus, the widely accepted standard to calculate pseudocapacitive and diffusive components (the pseudocapacitive component directly proportional to the voltage scan rate and the diffusive component directly proportional to the square root of the voltage scan rate) should not be used without caution. This explains the strange behavior seen in Figures S7e, f, where the MCMB peak current is seen to either plateau or decrease with scan rate at higher scan rates.
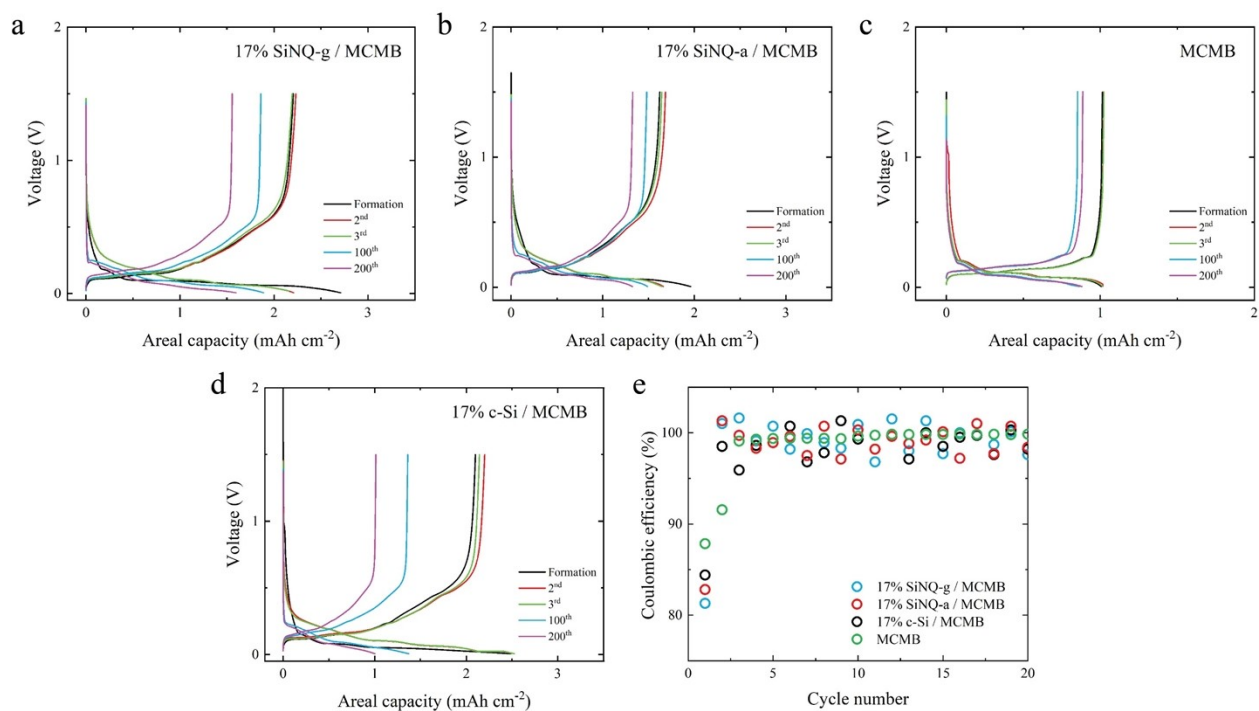
Figure S9: Charge-discharge profile of anode half cells with an active material comprising (a) 17% SiNQ-g/MCMB, (b) 17% SiNQ-a/MCMB, (c) pure MCMB graphite, (d) 17% c-Si/MCMB, and (d) their corresponding Coulombic efficiency for the first 20 cycles.
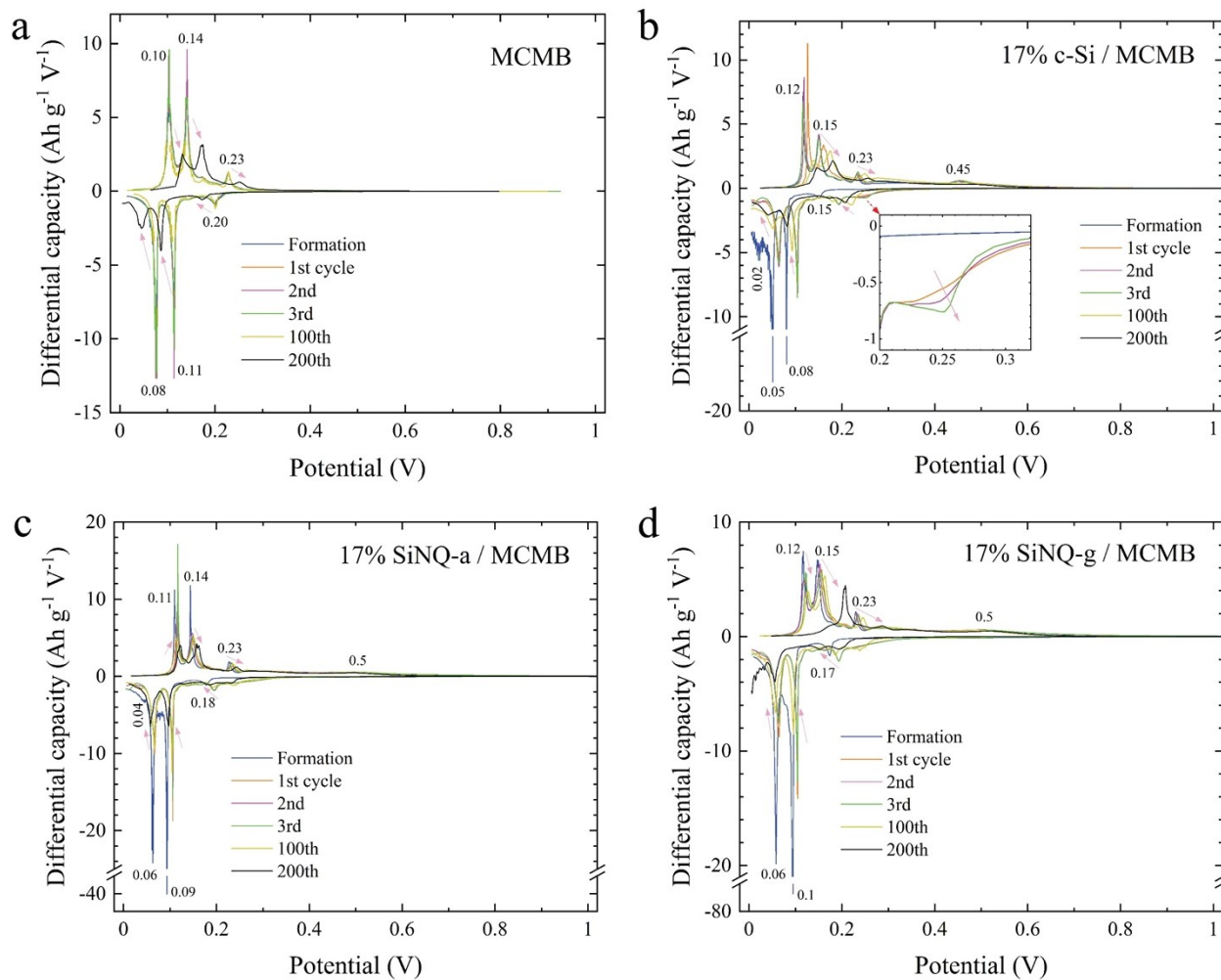
Figure S10: Differential capacity plots corresponding to the formation, 1st, 2nd, 3rd, 100th, and 200th cycles for all studied anodes. The characteristic peaks and their shift over cycling are marked in anodic and cathodic curves.
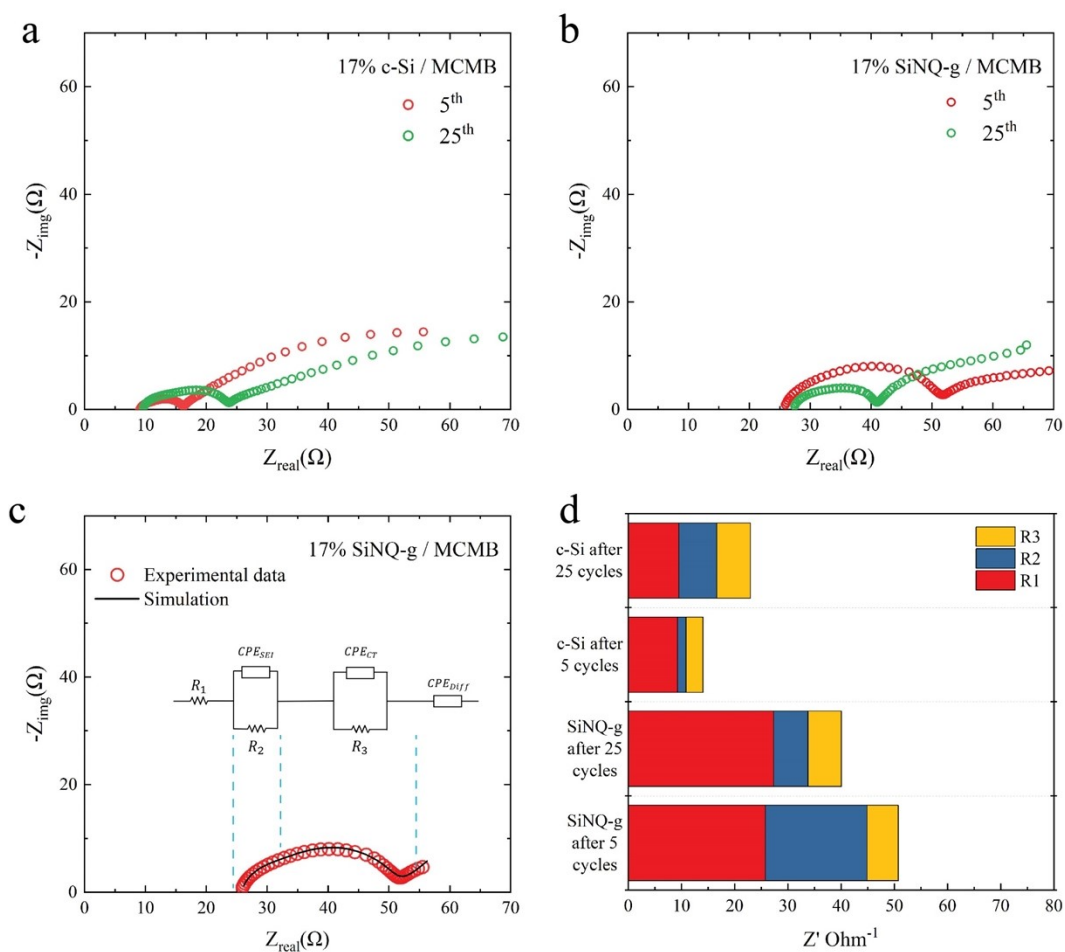
Figure S11: Electrochemical impedance spectroscopy results; Nyquist plots of (a) 17% c-Si/MCMB and (b) 17% SiNQ-g/MCMB electrodes after cycles 5 and 25. The equivalent Randles circuit used for modeling the EIS spectra is presented in (c) as an example of an experimental and simulated Nyquist plot. Impedance values derived from fitting models are plotted in (d).
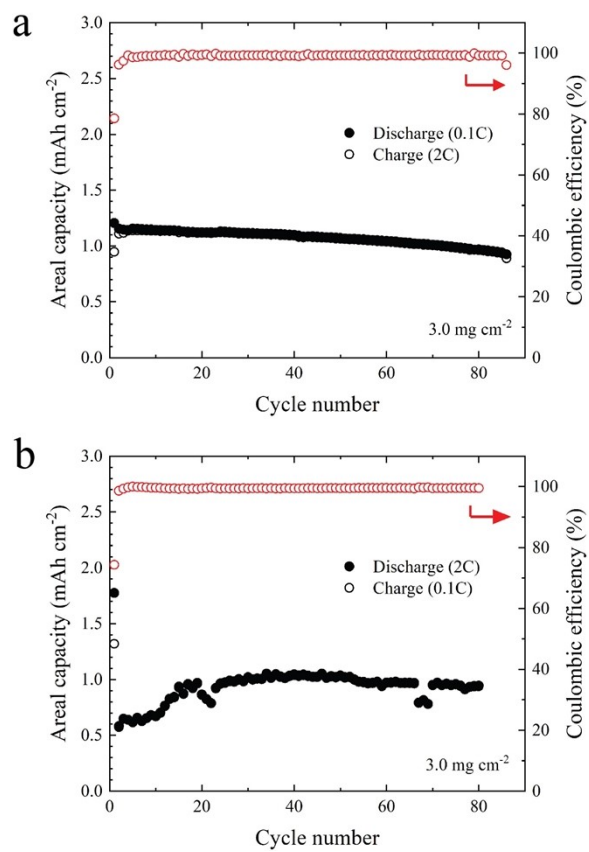
Figure S12: Electrochemical cycling of 17% SiNQ-g/MCMB electrodes at high current densities. (a) discharging at 0.1C and charging at 2C, and (b) discharging at 2C and charging at 0.1C. Half cells were cycled between 1.5 V and 0.005 V (1C = 900 mA g⁻¹). The formation cycle was performed at 0.05C.
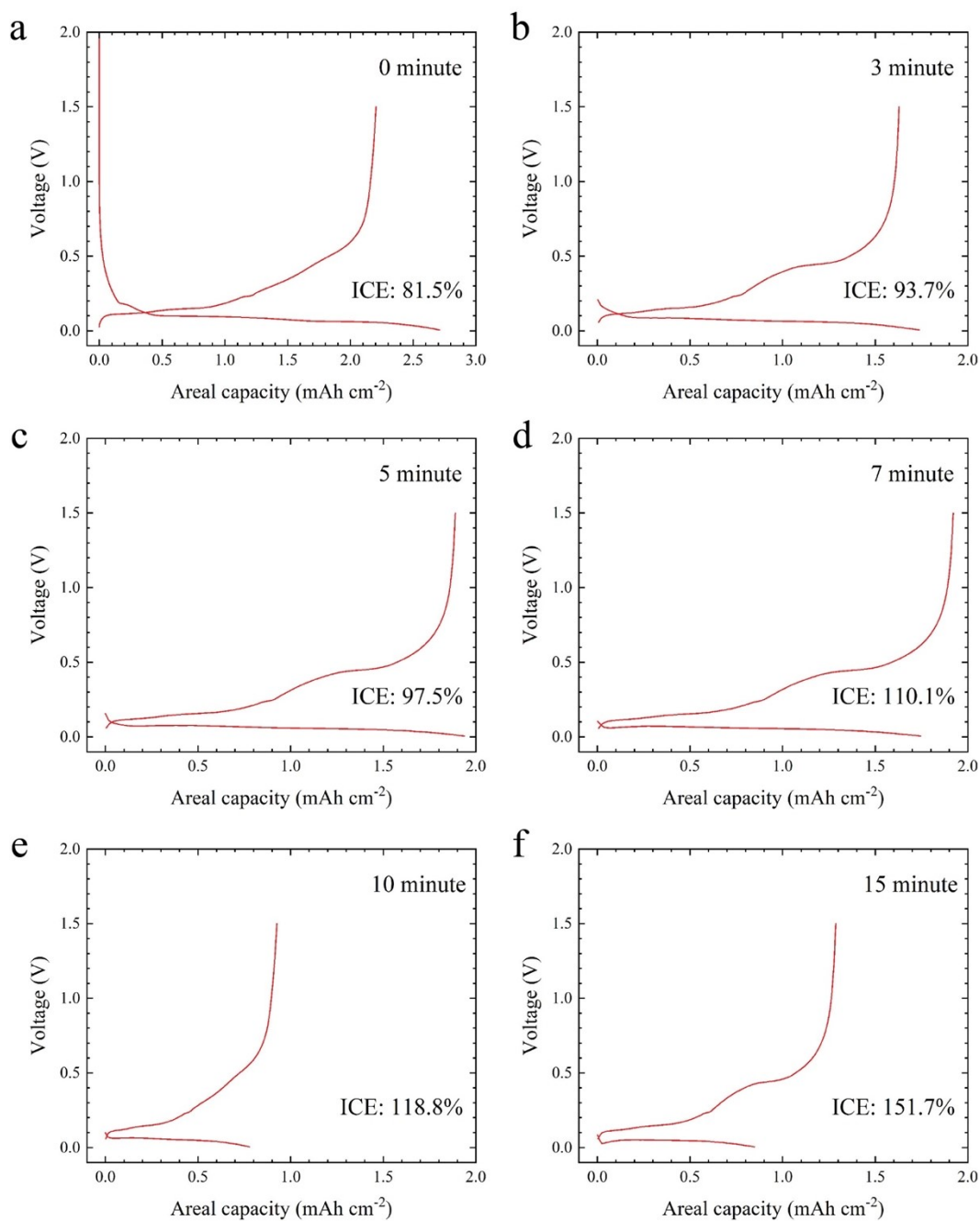
Figure S13: Initial charge-discharge profiles for 17% SiNQ-g/MCMB anodes pre-lithiated for different durations.

Table S1: A literature review of the electrochemical performance of Si-graphite electrodes from aqueous slurries.

Anode				Electrolyte	Half-cell testing condition	Capacity retention (%)	Ref
Active material	Composition	Si content in active material (wt.%)	Active mass loading (mg cm^{-2})				
c-Si/ MCMB graphite	Si/MCMB/ LiPAA/Super P (15:73:10:2)	17	4.5	1M LiPF$_6$ EC:DMC (1:1) + 10% FEC	0.005–1.5 V 90 mA g^{-1}	40%, 200 cycles	This work
SiNQ-g/ MCMB graphite	SiNQ-g/MCMB/ LiPAA/Super P (15:73:10:2)	17	4.5	1M LiPF$_6$ EC:DMC (1:1) + 10% FEC	0.005–1.5 V 90 mA g^{-1}	85%, 100 cycles 75%, 200 cycles	This work
Commercial Si/ Graphite	Si/CNT/graphite/CMC/ PAA/Super P (8.8:3.2:68:7.5:7.5:10)	15	1.2	1 M LiPF$_6$ EC:DMC (3:7)	0.01–1.5 V 120 mA g^{-1}	68%, 50 cycles	[2]
Si-C/ Graphite	Si/C/graphite/PAA/ Super P (12:20:48:10:10)	15	1.5	1M LiPF$_6$ EC:DMC (3:7)	0.01–2.0 V 130 mA g^{-1}	80%, 100 cycles	[3]
Si(CVD)@Carbon/ Flaked graphite	Si/C/graphite/CMC/ Super P (12:8:60:5:15)	15	1.92	1 M LiPF$_6$ EC:EMC:DMC (1:1:1) + 5% FEC + 0.5% VC	0.01–1.2 V 200 mA g^{-1}	94.3%, 100 cycles	[4]
Nano-Si@C/ Graphite	Si/C/graphite/CMC&S BR/Carbon black (11.68:31.68:36.64:10: 10)	14.6	1.5 - 2.0	1 M LiPF$_6$ EC:DEC (1:1) + 10% FEC	0.005–1.5 V 120 mA g^{-1}	75.2%, 150 cycles	[5]
SiNPs/ Graphite	Si/Graphite/ LiPAA/Super P (15:73:10:2)	17	2.5	1.2 M LiPF$_6$ EC:EMC (3:7) +10% FEC	0.05–1.5 V 87.5 mA g^{-1}	66.4%, 100 cycles	[6]

References

1   N. Ding, J. Xu, Y. X. Yao, G. Wegner, X. Fang, C. H. Chen and I. Lieberwirth, *Solid State Ionics*, 2009, **180**, 222–225.

2   H. Jo, J. Kim, D. T. Nguyen, K. K. Kang, D. M. Jeon, A. R. Yang and S. W. Song, *J. Phys. Chem. C*, 2016, **120**, 22466–22475.

3   S. Y. Kim, J. Lee, B. H. Kim, Y. J. Kim, K. S. Yang and M. S. Park, *ACS Appl. Mater. Interfaces*, 2016, **8**, 12109–12117.

4   Z. Yan, S. Yi, X. Li, J. Jiang, D. Yang and N. Du, *Mater. Today Energy*, 2023, **31**, 1–10.

5   S. Jeong, X. Li, J. Zheng, P. Yan, R. Cao, H. J. Jung, C. Wang, J. Liu and J. G. Zhang, *J. Power Sources*, 2016, **329**, 323–329.

6   P. F. Cao, M. Naguib, Z. Du, E. Stacy, B. Li, T. Hong, K. Xing, D. N. Voylov, J. Li, D. L. Wood, A. P. Sokolov, J. Nanda, T. Saito, B. Hu, S. Jiang, I. A. Shkrob, J. Zhang, S. E. Trask, B. J. Polzin, A. Jansen, W. Chen, C. Liao, Z. Zhang and L. Zhang, *J. Power Sources*, 2019, **10**, 3470–3478.